The Double Detonation of a Double-degenerate System, from Type Ia Supernova Explosion to its Supernova Remnant

Gilles Ferrand, Ataru Tanikawa, Donald C. Warren, Shigehiro Nagataki, Samar Safi-Harb, Anne Decourchelle

The Astrophysical Journal, 930:92 (17pp), 2022 May 1 https://doi.org/10.3847/1538-4357/ac5c58

The Double Detonation of a Double-degenerate System, from Type Ia Supernova Explosion to its Supernova Remnant

Gilles Ferrand[1,2], Ataru Tanikawa[3], Donald C. Warren[2], Shigehiro Nagataki[2,1], Samar Safi-Harb[4], and Anne Decourchelle[5,6]

[1] Astrophysical Big Bang Laboratory (ABBL), RIKEN Cluster for Pioneering Research, Wakō, Saitama, 351-0198 Japan; gilles.ferrand@riken.jp
[2] RIKEN Interdisciplinary Theoretical and Mathematical Sciences Program (iTHEMS), Wakō, Saitama, 351-0198 Japan
[3] Department of Earth Science and Astronomy, College of Arts and Sciences, The University of Tokyo, Meguro, Tokyo, 153–8902 Japan
[4] Department of Physics & Astronomy, University of Manitoba, Winnipeg, MB R3T 2N2, Canada
[5] Université Paris-Saclay, CEA, CNRS, AIM, F-91191 Gif-sur-Yvette, France
[6] Université de Paris, AIM, F-91191 Gif-sur-Yvette, France
Received 2021 November 24; revised 2022 January 31; accepted 2022 February 5; published 2022 May 6

Abstract

Type Ia supernovae (SNe) are believed to be caused by the thermonuclear explosion of a white dwarf (WD), but the nature of the progenitor system(s) is still unclear. Recent theoretical and observational developments have led to renewed interest in double-degenerate models, in particular the "helium-ignited violent merger" or "dynamically driven double-degenerate double-detonation" (D^6). In this paper we take the output of an existing D^6 SN model and carry it into the supernova remnant (SNR) phase up to 4000 yr after the explosion, past the time when all the ejecta have been shocked. Assuming a uniform ambient medium, we reveal specific signatures of the explosion mechanism and spatial variations intrinsic to the ejecta. The first detonation produces an ejecta tail visible at early times, while the second detonation leaves a central density peak in the ejecta that is visible at late times. The SNR shell is off-center at all times, because of an initial velocity shift due to binary motion. The companion WD produces a large conical shadow in the ejecta, visible in projection as a dark patch surrounded by a bright ring. This is a clear and long-lasting feature that is localized, and its impact on the observed morphology is dependent on the viewing angle of the SNR. These results offer a new way to diagnose the explosion mechanism and progenitor system using observations of a Type Ia SNR.

Unified Astronomy Thesaurus concepts: Supernovae (1668); Supernova remnants (1667); Hydrodynamical simulations (767)

Supporting material: animations, interactive figure

1. Introduction

Supernovae (SNe) mark the end of the life of stars, and are one key step in the life cycle of elements in the Galaxy. Type Ia SNe have attracted a lot of attention, for enabling the discovery of cosmic acceleration (see Garnavich 2017, for a review). SNe Ia are thought to be the thermonuclear explosion of a white dwarf (WD), although they come in many types (Jha et al. 2019) and their progenitor system(s) are still unclear (Ruiter 2020). Many scenarios have been proposed for the explosion (Hillebrandt et al. 2013), a basic idea being that the WD is part of a binary system so that it can increase its mass via accretion or merger.

There is no consensus on the nature of companion stars of exploding WDs. The companion star may be a nondegenerate star—the single degenerate scenario (Whelan & Iben 1973; Nomoto 1982), another WD—the double-degenerate scenario (Iben & Tutukov 1984; Webbink 1984), or the core of an asymptotic giant star—the core degenerate scenario (Kashi & Soker 2011). Recent observations have put some constraints on the single degenerate scenario. No red-giant star has been found in the pre-explosion images of SN 2011fe and 2014J (Li et al. 2011; Kelly et al. 2014, respectively), which are the nearest type Ia SNe observed in the past decade. No surviving stellar companions were convincingly detected in the remnants of nearby Ia SNe (see Ruiz-Lapuente 2019, for a review). On the other hand, some type Ia SNe may indicate the presence of nondegenerate companion stars, such as PTF11kx (Dilday et al. 2012), iPTF14atg (Cao et al. 2015), and SN 2012cg (Marion et al. 2016). These observational results suggest that type Ia SNe may have multiple origins (Hillebrandt et al. 2013).

The double-degenerate scenario is one of the promising scenarios for type Ia SNe. In this scenario, the exploding WD may be a near-Chandrasekhar-mass explosion with high central density, or a sub-Chandrasekhar-mass explosion with low central density. Near-Chandrasekhar-mass explosion has been thought to be difficult theoretically, because such a WD converts its composition from carbon–oxygen to oxygen–neon–magnesium (Saio & Nomoto 1985; Schwab et al. 2012; Ji et al. 2013), and collapses to a neutron star rather than exploding as a type Ia SN (Nomoto & Kondo 1991). Various sub-Chandrasekhar-mass explosion models have been suggested. Although the violent merger model can successfully produce type Ia SNe (Pakmor et al. 2011, 2012; Tanikawa et al. 2015), the total mass of two WDs should be larger than the Chandrasekhar mass (Sato et al. 2015, 2016), which means that the event rate is smaller than the type Ia SN rate (Maoz et al. 2014). Another model, called the "helium-ignited violent merger" or "dynamically driven double-degenerate double-detonation" (hereafter, D^6) allows the total mass of the two WDs to be less than the Chandrasekhar mass (Guillochon et al. 2010; Pakmor et al. 2013). The D^6 scenario is supported by the

recent discovery of a hypervelocity WD by Shen et al. (2018b), which is expected to be left as a by-product of the explosion. Thus, the D^6 model has become a promising model for type Ia SNe.

This has motivated many researchers to examine the double detonation of a sub-Chandrasekhar-mass WD with respect to its explodability, nucleosynthesis, and observability (e.g., Shen et al. 2018a, 2021; Gronow et al. 2020, 2021; Polin et al. 2019, 2021; Pakmor et al. 2021). These studies have mainly focused on the exploding WD, not the surviving WD. Papish et al. (2015) and Tanikawa et al. (2018, 2019) have shown that D^6 SN ejecta exhibit nonspherical features because of the presence of the surviving WD. If such nonspherical features can survive until the remnant phase, it would be inconsistent with spherically symmetric objects. On the other hand, SN ejecta may become spherical through interaction with the interstellar medium (ISM). In addition, the chemical compositions of D^6 ejecta would be different from those of SN Ia ejecta with a nondegenerate companion star. In the D^6 scenario, ejecta can contain a significant amount of carbon and oxygen, stripped from the companion WD (Tanikawa et al. 2018, 2019). If the companion star is nondegenerate, the ejecta may contain hydrogen stripped from a main-sequence or red-giant star, or helium in the case the companion is a helium star (Marietta et al. 2000; Pan et al. 2012; Liu et al. 2013; Boehner et al. 2017). It is unknown whether this difference is observable or not after SN ejecta interact with the ISM.

The supernova remnant (SNR) is the phase following the SN, made from the interaction of the ejecta with the circumstellar and/or interstellar matter (Reynolds 2017). In a young, ejecta-dominated SNR, the shell of shocked matter is bounded by two shocks: the forward shock (FS) developing ahead of the supersonic ejecta, and the reverse shock (RS) forming inside the ejecta as they are decelerated. The shocked matter (shocked ejecta and shocked ISM) is heated to X-ray-emitting temperatures, for thousands of years (Vink 2017). The interface between the ejecta and the ISM, a contact discontinuity (CD), is unstable and subject to the Rayleigh–Taylor instability (RTI). This shapes the SNR independently of its initial conditions (the explosion) and boundary conditions (the ISM).

In this work we are specifically investigating the impact of the initial explosion on the SNR morphology. A D^6 SN is rather symmetric, except for the marked imprint from the companion WD. In the study of thermonuclear explosions in binary systems, there has been a number of works that considered the interaction of the ejecta with the companion star, in terms of the impact on the SN emission, or the fate of the companion (e.g., Marietta et al. 2000; Pakmor et al. 2008; Kasen 2010; Liu et al. 2013; Maeda et al. 2014; Boehner et al. 2017; Dessart et al. 2020; Zeng et al. 2020; Liu & Zeng 2021). There have also been several searches for surviving companions in SNRs (Ruiz-Lapuente 2019), but looking for normal stars—an exception being Kerzendorf et al. (2018), who looked for a WD too, motivated by the theoretical study of Shen & Schwab (2017). A feature of the D^6 scenario is that the surviving companion is itself a WD.[7] In contrast only a few works have looked into the signature of a companion on the SNR—and all assuming normal stars for the companion (Lu et al. 2011; Vigh et al. 2011; García-Senz et al. 2012; Gray et al. 2016). In this paper we investigate for the first time the imprints on the SNR with a WD companion and follow the evolution up to when all the ejecta have been shocked.

[7] A companion WD could also exist in a single degenerate scenario with the spin-up/spin-down mechanism (Di Stefano et al. 2011; Justham 2011; Hachisu et al. 2012; Benvenuto et al. 2015).

Table 1
Model Parameters

primary's mass	$M_1 = 1.0\ M_\odot$ (95% CO + 5% He)
secondary's mass	$M_2 = 0.6\ M_\odot$ (100% CO)
orbital separation	$d_{12} = 1.6 \times 10^4$ km
primary's orbital velocity	$v_1 = 1100$ km s^{-1}
secondary's orbital velocity	$v_2 = 1800$ km s^{-1}
angular size of secondary seen from primary	$2\theta_2 = 44°$, $\Omega_2 = 0.46$ sr
ejecta mass	$M_{\rm ej} = 0.97\ M_\odot$
total kinetic energy	$E_{\rm SN} = 1.11 \times 10^{51}$ erg
ISM density	$\rho_{\rm ISM} = 0.1\ m_p.{\rm cm}^{-3}$

Our approach is to run numerical simulations from the 3D SN to the 3D SNR. We already applied it to the canonical model for a Type Ia SN: the explosion of a Chandrasekhar-mass WD (Ferrand et al. 2019, hereafter Paper I), examining the impact of the ignition and of the propagation of the flame (Ferrand et al. 2021, hereafter Paper II). In Paper I we showed that, assuming a uniform ambient medium, the impact of the SN on the SNR may still be visible after hundreds of years. Furthermore, in Paper II we showed that the details of the explosion mechanism matter: the more asymmetric ignition setups produce more asymmetric remnants, and in a way that is different for deflagrations versus detonations. In this paper we are investigating a different kind of Type Ia model: the double detonation of a WD in a double-degenerate system.

The paper is organized as follows. In Section 2 we summarize the methods for carrying out the numerical simulations and analyzing their results. In Section 3 we present the results on the SNR morphology, using a selection of representative maps. In Section 4 we discuss implications for observations of young, nearby SNRs. In Section 5 we conclude and outline our perspectives with the D^6 model.

2. Method

Our simulation is done in two steps, the SN explosion per se, already published, and the subsequent SNR evolution, presented in this paper.

The supernova—Our D^6 SN model is described in detail in Tanikawa et al. (2018). The main model parameters are summarized in Table 1. The simulation was made with a smoothed-particle hydrodynamics (SPH) code, using a Helmholtz equation of state (Timmes & Swesty 2000), and coupled with the nuclear reaction network Approx13 (Timmes et al. 2000). As for the initial conditions, we considered a binary system with WDs of mass $1.0M_\odot$ for the primary and $0.6M_\odot$ for the secondary. According to Shen et al. (2018a; see their Figure 5) a $1.0M_\odot$ WD produces about the mass of ^{56}Ni required to power a typical SN Ia, while lower masses would produce underluminous events and higher masses would produce overluminous events. As for the mass of the secondary, the way it impacts the explodability of the primary is not settled, but it should not affect the result of the explosion of the primary. The primary is made of 95% CO in its core and 5% He in its shell, while the secondary is pure CO with equal C and O, in mass (there is the possibility that the secondary also

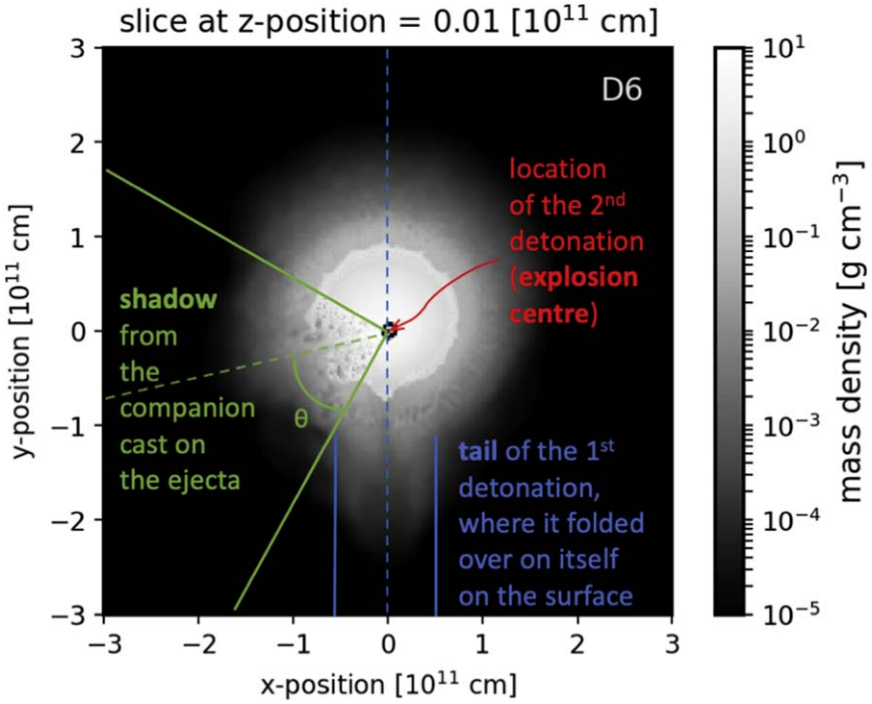

Figure 1. Slice of the ejecta of the D^6 explosion, annotated with its specific features. This figure was made from the output data at 50 s of the SN simulation published in Tanikawa et al. (2018), which are the input data of the SNR simulation presented in this paper. The quantity plotted is the mass density of the ejecta of the exploded primary WD. The slice is taken in the *x*–*y* plane, through the origin of the *z*-axis. The tail visible at the bottom (blue outline) is where the first detonation folded over on itself, on the surface of the primary WD, opposite to the ignition point. The second detonation, which destroyed the primary WD, happened near its center (red arrow). The shadow that was cast in the ejecta of the primary WD by the presence of the secondary WD is visible on the bottom left side (green outline). It has a conical shape, of half-opening angle θ. The inner part of it, along the cone axis, is contaminated with material stripped from the secondary WD. (At the scale of this plot, the two WDs can barely be distinguished, their separation is of the order of the thickness of the solid lines.) A Sketchfab-based interactive version of the D^6 SN at 50 s is available in the online Journal. This version shows a set of isocontours of the mass density, rendered as semitransparent surfaces: four contours in the inner ejecta, at levels ranging from 8% to 1% of the maximum value from red to yellow, and two contours in the outer layers, at levels 10^{-4} and 10^{-5} in white. This view highlights the conical shadow cast by the companion WD, and also shows the tail.

has an He layer). Although the exact composition of the primary WD does affect the yields somewhat, it does not alter the total kinetic energy of the ejecta (Sim et al. 2010), which controls the dynamics of the remnant phase. The two WDs orbit each other with a semimajor axis of 1.6×10^4 km. The first detonation is ignited by adding a hot spot on the surface of the primary. The hot spot is located in the orbital plane of the binary system, and in the propagating direction of the primary WD.[8] The first detonation develops over the He layer, and folds over on itself in $t = 1.25$ s, making a splash at the opposite point. The shock is then channeled into the WD, and it converges at the center at $t = 1.625$ s, triggering the second detonation, the thermonuclear explosion that disrupts the primary WD. The explosion generates a kinetic energy of $\simeq 10^{51}$ erg and synthesizes a mass of ^{56}Ni of 0.54 $M_\odot$.

The interaction of the primary WD's ejecta with the secondary WD produces distinctive features in otherwise spherically symmetric ejecta, as seen in Figure 5 in Tanikawa et al. (2018) and our annotated Figure 1. The main feature is a wide shadow in the ejecta (solid angle $\Omega = 1.8$ sr, of conical shape with half-opening angle $\theta = 44.^\circ5$), a region of lower density and more irregular material, which was cast by the companion. A second feature is a narrow stream ($\Omega = 0.21$ sr, $\theta = 14.^\circ8$) of material that was stripped from the companion; in particular, low-velocity carbon and oxygen moving at $\simeq$3000 km s^{-1}. Such low-velocity oxygen can be seen in the nebular phase of SN 2010lp (Kromer et al. 2013; Taubenberger et al. 2013) and iPTF14atg (Kromer et al. 2016), two SN 2002es-like subluminous type Ia SNe. Also visible in Figure 1 in the outer, less dense region, is an extended tail, along the line where the first detonation folded over on itself on the surface of the primary WD. Another feature of the D^6 explosion is that the ejecta have a velocity shift of $\sim$1000 km s^{-1}. In our simulation the secondary WD survives the explosion of the primary (it may or may not explode; see Tanikawa et al. 2019). It has a velocity of $\simeq$1700 km s^{-1}, that is, traveling 1 pc every 575 yr, in a direction perpendicular to the axis of the conical shadow, and it has a peculiar composition from ejecta contamination. An interactive 3D model of the ejecta is available online,[9] made from isocontours of the mass density, which shows the conical shadow, as well as the tail.

The supernova remnant—Results of the SN simulation at 50 s were mapped to a Cartesian grid of physical size 6×10^{11} cm with spatial resolution 256^3, and loaded into our custom version of the Eulerian hydrodynamics code Ramses (Teyssier 2002) to conduct the SNR simulations. The ability of the code to follow SNR dynamics was demonstrated in our earlier works focused on particle acceleration (Ferrand et al. 2010, 2012, 2014). For D^6, the companion itself is not included in the SNR simulation (its size is $\lesssim 2 \times 10^9$ cm, about the size of a single grid cell); only its impact on the ejecta is considered (the direct interaction

[8] Guillochon et al. (2010) obtained that the first detonation starts at the end point of the accretion stream, but Pakmor et al. (2013) obtained that it starts far from this end point, which suggests that it could start at any point on the orbital plane.

[9] On Sketchfab at skfb.ly/6VXwU.

between the companion WD and the ejecta is finished by that time). The method is the same as in Papers I and II. Considering the initial quasi self-similarity, we first scale up the hydro profiles from 50 s to 1 day, and start the SNR simulation at 1 day. We follow the evolution up to 4000 yr after the explosion, which is after the RS has shocked all of the ejecta and reached the SNR center. This is a more advanced age than in previous papers, because we observed longer-lasting features with D[6]. The SNR remains in an adiabatic phase of evolution, with our parameters the radiative snowplow phase would start at about 50,000 yr (Cioffi et al. 1988). The SNR simulation is performed in a comoving grid: factoring out the global expansion of the SNR over that period of time allows us to focus numerical resolution on the dynamics of the shocked ejecta.[10] For reference the box size is 4.5×10^{-4} pc at 1 day, 5.6 pc at 100 yr, 40 pc at 4000 yr. In order to separate the effects of the explosion and of any structure in the ambient medium, we assume a homogeneous ISM of number density 0.1 cm^{-3} to have dynamics roughly similar to Tycho's SNR. The overall hydrodynamic evolution of the SNR is controlled by three characteristic scales for the radius, velocity, and time (Dwarkadas & Chevalier 1998; Warren & Blondin 2013):

$$r_{\rm ch} = \left(\frac{3M_{\rm ej}}{4\pi\rho_{\rm ISM}}\right)^{1/3} \simeq 4.54 \text{ pc}, \quad (1)$$

$$u_{\rm ch} = \left(\frac{2E_{\rm SN}}{M_{\rm ej}}\right)^{1/2} \simeq 10\,700 \text{ km s}^{-1}, \quad (2)$$

$$t_{\rm ch} = \frac{r_{\rm ch}}{u_{\rm ch}} \simeq 412 \text{ yr}, \quad (3)$$

where $M_{\rm ej}$ is the mass of the ejecta, $E_{\rm SN}$ is the (kinetic) explosion energy, and $\rho_{\rm ISM}$ is the mass density of the ISM.

The analysis of the SNR morphology is performed as explained in the previous papers. At each step we track three surfaces of particular interest: RS, CD, FS. At run time we extract in 3D the surface of each wave front and record its radius from the explosion center. Treating the latter as a function on a sphere, we expand its relative variations in spherical harmonics and compute the angular power spectrum. The simulation was also done with smooth initial conditions (labeled 1Di, versus 3Di for the full initial conditions), made by averaging the mass density over all angles, in order to assess what happens from the SNR phase only.

3. Results

Our simulation shows the expected dynamical evolution for a young SNR: the formation of a shell of dense and hot matter bounded by the RS and the FS. This is the region where thermal emission is produced in the X-ray band, which can be observed with space-borne telescopes. In Figure 2 we show a 3D view of the SNR shell, at an age of 500 yr for illustration. In this plot only the shocked matter is shown, the ejecta shocked by the RS (green hues), and the ISM shocked by the FS (purple hue). We use both isocontours and a volume rendering of the mass density. Part of the shell has been removed to show its interior. The typical field of Rayleigh–Taylor fingers is visible all around. The shell is globally symmetric except for a flat edge of the RS (at the bottom of the plot), with reduced RTI between the shocks. As we will see more clearly in the subsequent figures, this is the imprint from the shadow cast by the companion WD in the ejecta of the exploded WD. We also note a region with more marked fingers (toward the bottom right corner of the plot); this corresponds to the tail where the first detonation folded over on itself. Another 3D model of the SNR is available online,[11] made from isocontours of the ejecta tracer, which shows the morphology of the RT fingers in the shell of shocked matter, and is interactive.

In the following, in order to explain the morphological evolution we use three different kinds of plots: (i) 2D slices of the mass density, of all the matter, to reveal the inner structure of the SNR (Figure 3); (ii) 2D projections along a line of sight of the density squared, which serves as a proxy of the thermal X-ray emission (Figure 4); and (iii) spherical maps and angular spectra, which show the surface of the wave fronts and quantify their angular content (Figures 5, 6, 7). To make it easier to identify the features from the explosion, we generated color-coded masks that show the shadow cone from the WD companion (green), and the tail where the first detonation converges at the surface of the exploding WD (blue), versus the regular ejecta (red). For each of the three series of figures listed above, the masks are generated in the same way as the maps: a slice (not time-dependent, as it is purely geometrical), a sum in projection weighted by the quantity of interest (slightly time-dependent, as the quantity may be evolving), the intersection with the wave fronts (slowly time-dependent, as the waves are moving). For the slice and projection maps, on each figure we show the results along three directions (the three principal axes x, y, z of our simulation box), so as to grasp the entire morphology of the SNR. By design the spherical maps show the entire surface of the SNR at once.

Slices—Slices of the mass density are shown in Figure 3 at select times, and a movie from 1 yr to 4000 yr by steps of 1 yr is available online. The projected position of the companion WD, assuming ballistic motion, is indicated by a white cross; it is still inside the SNR by the end of the simulation. Over time, the characteristic shell structure develops, bounded by the RS and FS. The RTI grows on top of the irregular ejecta boundary. While the instability is in the linear phase, the fingers grow exponentially in time, the resolution of our simulation does not allow us to probe this phase in detail. According to Schulreich & Breitschwerdt (2022), the instability saturates and enters the nonlinear phase by the time the extent of the perturbations has reached half their wavelength, which in our simulation happens within the first few years of the SNR evolution. For hundreds of years after, we see that the evolution of the RTI fingers is essentially self-similar. After about a thousand years, we see that the fingers start merging with one another.

Looking at features from the explosion, we note the persistence of a dense region in the center of the remnant. The shell is off-center, as a result of the initial velocity shift—so the geometric center of the remnant is not the explosion point. There are two other prominent features that stem from the explosion. First, the tail from the first detonation is visible past the average shock surface. At early times (around a hundred years after the explosion) it looks like a protrusion, being ahead of the average FS surface, but actually it is present from the beginning and is being overtaken by the bulk of the expanding ejecta. This feature

[10] Numerical resolution affects our ability to capture the RTI: the instability always grows from the smallest scales available, up to larger scales over time. A resolution study was performed for the N100 model, and the overall trends on maps and angular spectra were found to be robust—see the discussion in Section 4.1 in Paper I.

[11] On Sketchfab at skfb.ly/oqoGX

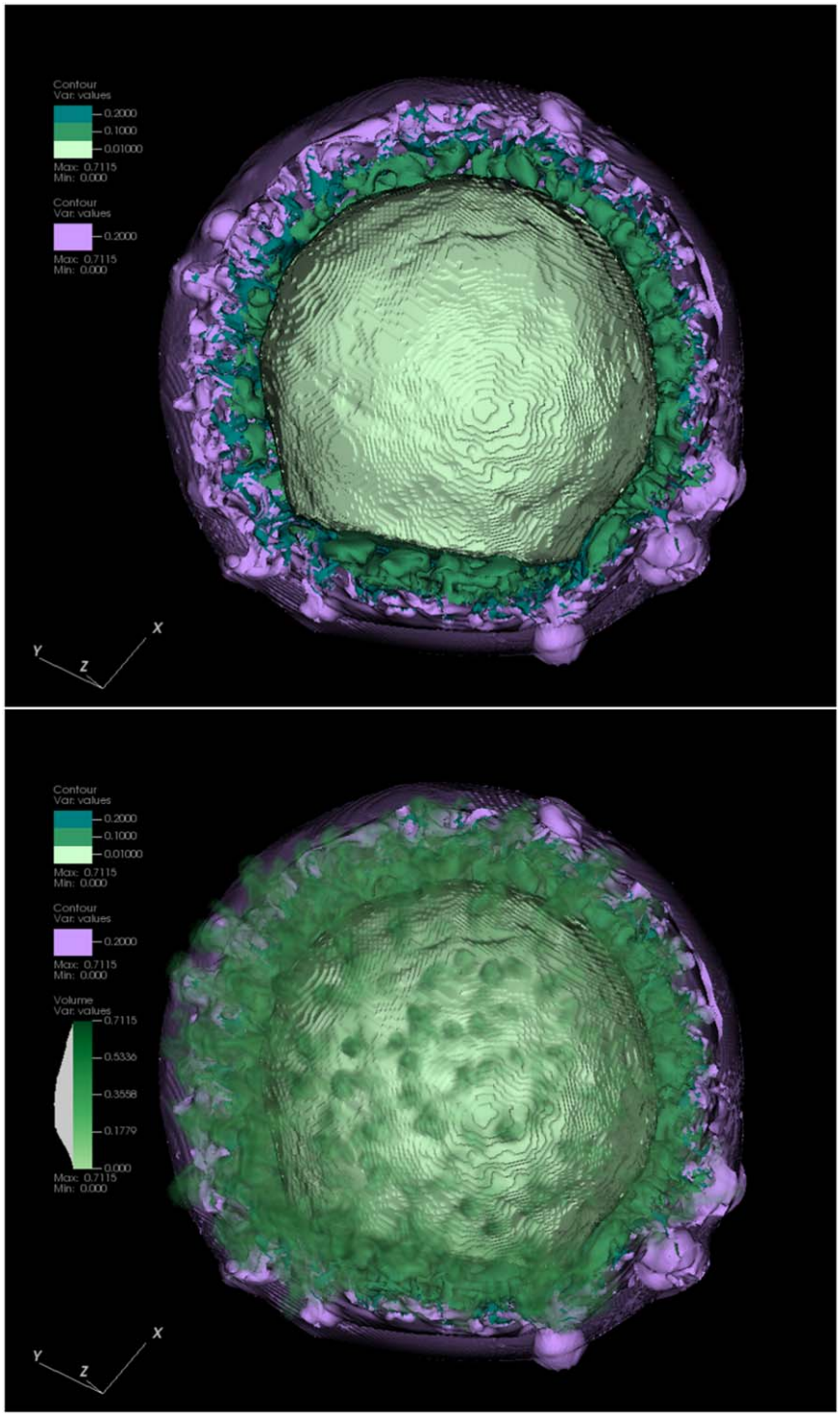

Figure 2. 3D view of the D^6 SNR at 500 yr. The solid contours are isocontours of the mass density. Green colors in the inner layers correspond to shocked ejecta, while purple colors in the outer layers correspond to shocked ambient matter. In both panels the contours are clipped to one half of the SNR to see its interior. In the bottom panel, a volume rendering of the mass density of the shocked ejecta is included, over the entire surface of the SNR. A Sketchfab-based interactive version of the D^6 SNR at 500 yr is available in the online Journal. This version shows isocontours of the ejecta tracer, in the shell of shocked matter. Layers of shocked ejecta are displayed in cool colors, from green at the RS to blue at the CD. Layers of shocked ISM are displayed in warm colors, from purple at the FS to red at the CD. The shocks, RS and FS, are rendered as semitransparent surfaces. This view highlights the morphology of the RTI fingers.

is mostly erased after a few hundred years. Second, the conical shadow from the companion WD is visible as a deformed RS. In this underdense region the RS is traveling faster, the net result after a few hundred years is that the shock front looks segmented, with a straight edge across the shadow. Also we note that the edges of the cone have enhanced RT fingers growth.

The RS moves inward inside the ejecta,[12] reaching the center at about $t = 2690$ yr. This time is expected to scale as

[12] For a distant observer, the motion of the RS is first outward and later inward, as the RS velocity overtakes the SNR expansion velocity. Regardless, the RS is continuously sweeping up additional mass and thus moving to lower mass coordinates.

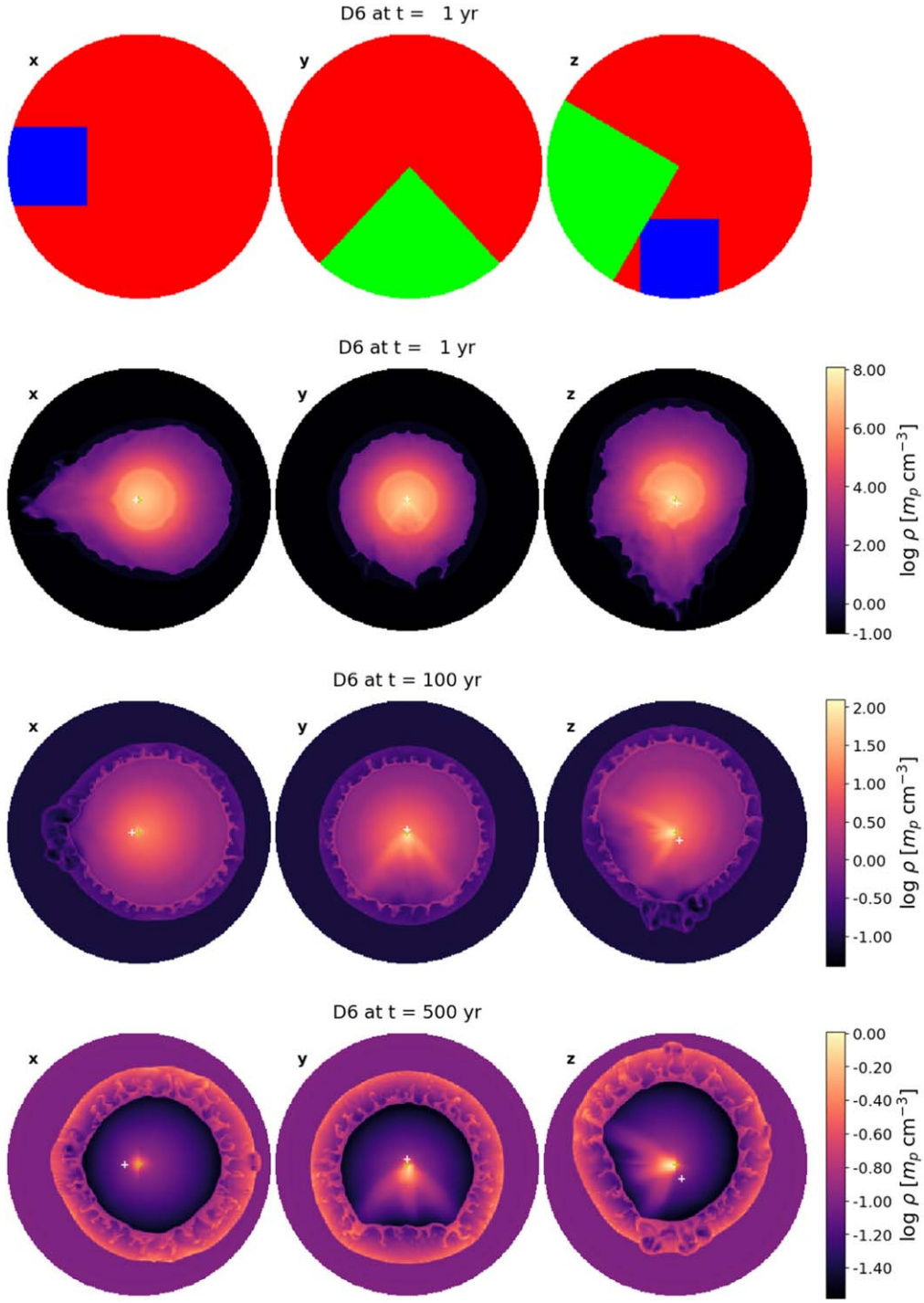

Figure 3. Slices of mass density at several times: 1 yr, 100 yr, 500 yr, 1000 yr, 2000 yr, 4000 yr after the explosion, along three different axes (principal axes x, y, z, of the simulation box). The box size is 0.14 pc at 1 yr, 5.6 pc at 100 yr, 15 pc at 500 yr, 22 pc at 1000 yr, 30 pc at 2000 yr, 36 pc at 3000 yr, 40 pc at 4000 yr. Note that the color scale is shared by the three slices, but adjusted independently at each time. The yellow cross marks the center of the exploded WD, the white moving cross marks the position of the surviving WD assuming it keeps its initial velocity (the WD is not resolved). An animated version of this figure is available online, showing the evolution from 1 yr to 4000 yr by steps of 1 yr (the duration is 1 minute 20 s). The first plot is a color-coded mask to aid in identifying the origin of the features: red = regular ejecta, green cone = shadow from the companion, blue cylinder = tail from the first detonation. These masks are only shown at $t = 1$ yr as they are not evolving over time. (An animation of this figure is available.)

Equation (3), that is, $E_{\rm SN}^{-1/2} M_{\rm ej}^{5/6} \rho_{\rm ISM}^{-1/3}$. In particular a lower/higher ambient density would mean a slower/faster evolution. After the RS has converged at the center, there is evidence of a rebound. This feature, which is robust in 3D (Petruk et al. 2021), will be studied in more detail in future work. The peculiar shape of the RS described above is visible all the way from its birth to its disappearance.

Projections—Projections of the density squared of the shocked ejecta, a proxy for their broadband thermal X-ray emission, are shown in Figure 4 at select times, and a movie

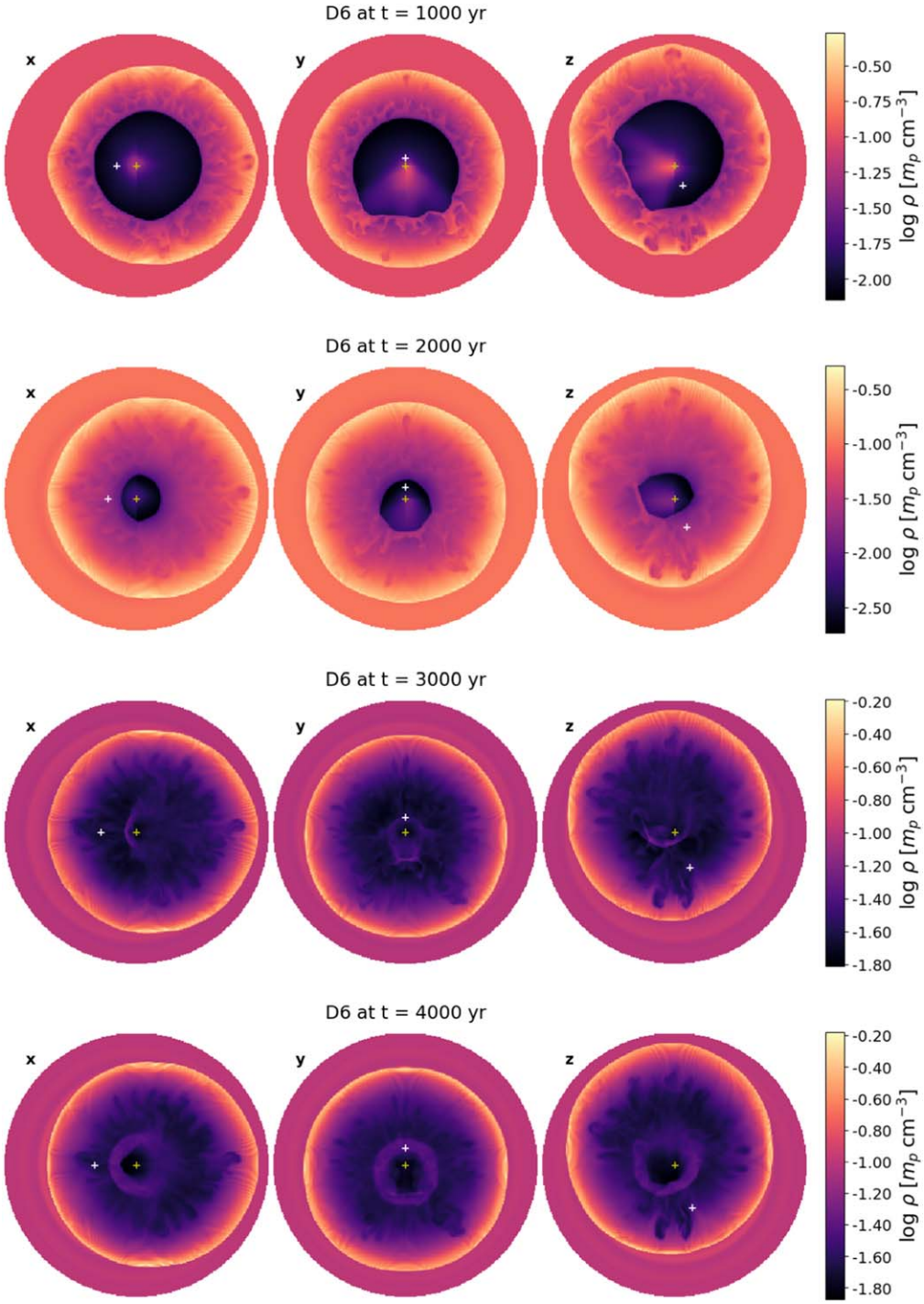

Figure 3. (Continued.)

from 1 yr to 4000 yr by steps of 1 yr is available online. Most of the small-scale structures visible on these maps come from the RTI. Over time the distance between the CD and the FS is increasing, and so in a comoving frame the ejecta appear to be shrinking in size. Only the shocked ejecta are shown, and so the central density peak is visible only when the RS reaches the center of the SNR. In projection, the tail from the first detonation is more difficult to see. The shadow from the companion is well visible; it appears as a dark disk surrounded by a brighter ring. The dark disk corresponds to an underdense region, while the bright ring corresponds to enhanced RTI. These features are actually getting more marked over time. They are visible until the rebound of the RS. As the shadow is a localized feature, the SNR morphology is different depending

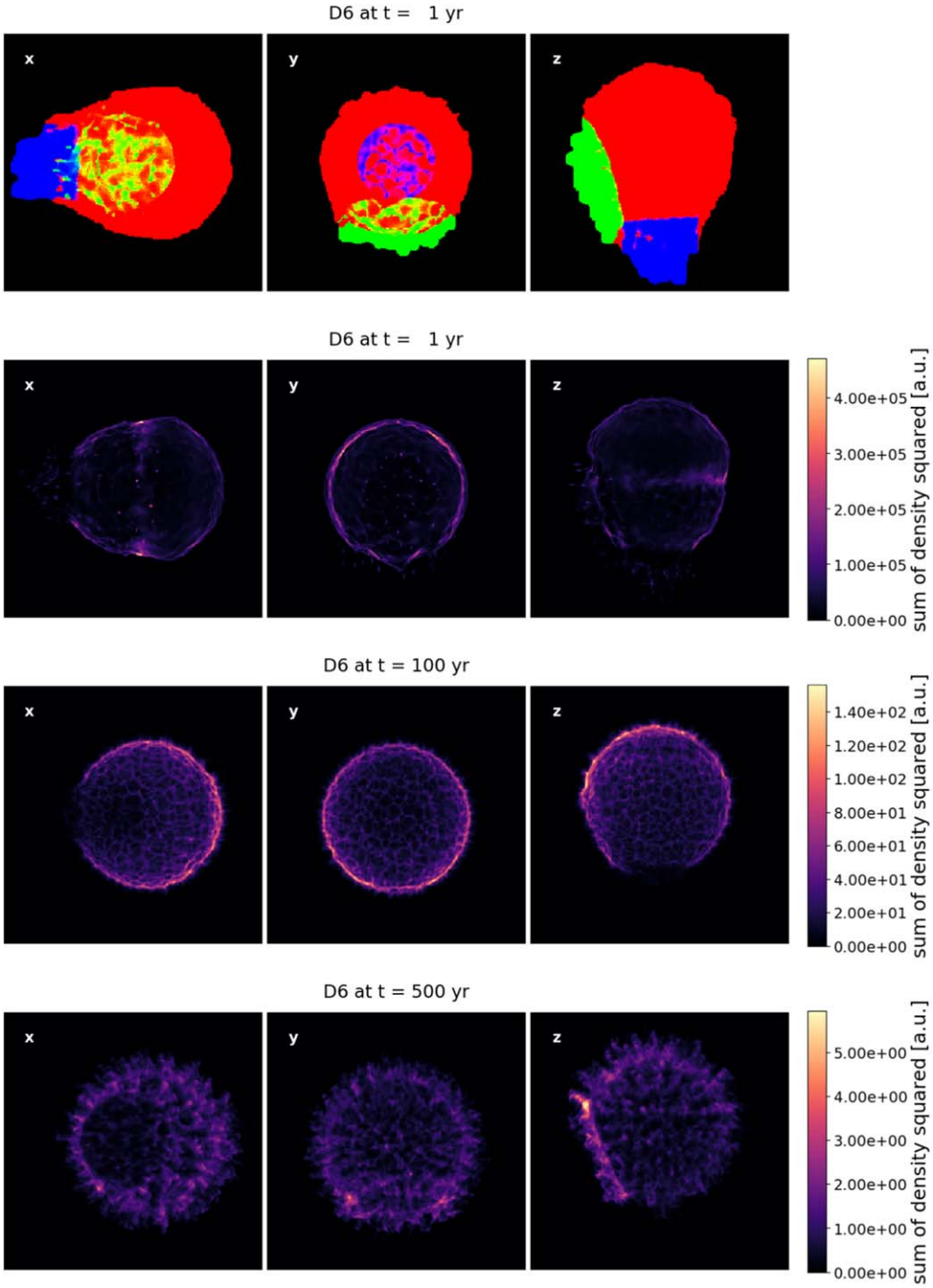

Figure 4. Projection of the mass density squared of the shocked ejecta at several times: 1 yr, 100 yr, 500 yr, 1000 yr, 2000 yr, 4000 yr after the explosion, along three different axes (principal axes x, y, z, of the simulation box). The box size at each time is the same as in the previous figure. Note that the color scale is shared by the three slices but is adjusted independently at each time. An animated version of this figure is available online, showing the evolution from 1 yr to 4000 yr by steps of 1 yr (the duration is 1 minute 20 s). The first plot is a color-coded mask to aid in identifying the origin of the features: red = regular ejecta, green cone = shadow from the companion, blue cylinder = tail from the first detonation. These masks are only shown at $t = 1$ yr as they are mildly evolving over time.

(An animation of this figure is available.)

on the direction of observation. Along the x-axis one is looking almost along the conical axis and so one sees the entire darker disk, along the y-axis one is looking at some angle and sees a bright ellipse, and along the z-axis one is looking sideways and sees a bright bar on the edge.

Initially the shocked ejecta dominate the overall shocked mass and thus the thermal X-ray emission, but eventually the shocked ISM dominates in mass.[13] When adding the contribution for the shocked ISM using the same proxy of

[13] For reference, the time at which the swept-up ISM mass is equal to the ejected mass, called the Sedov–Taylor time, is $t_{ST} = 465$ yr for our assumed parameters. The SNR dynamics will follow the Sedov–Taylor solution for $t \gg t_{ST}$.

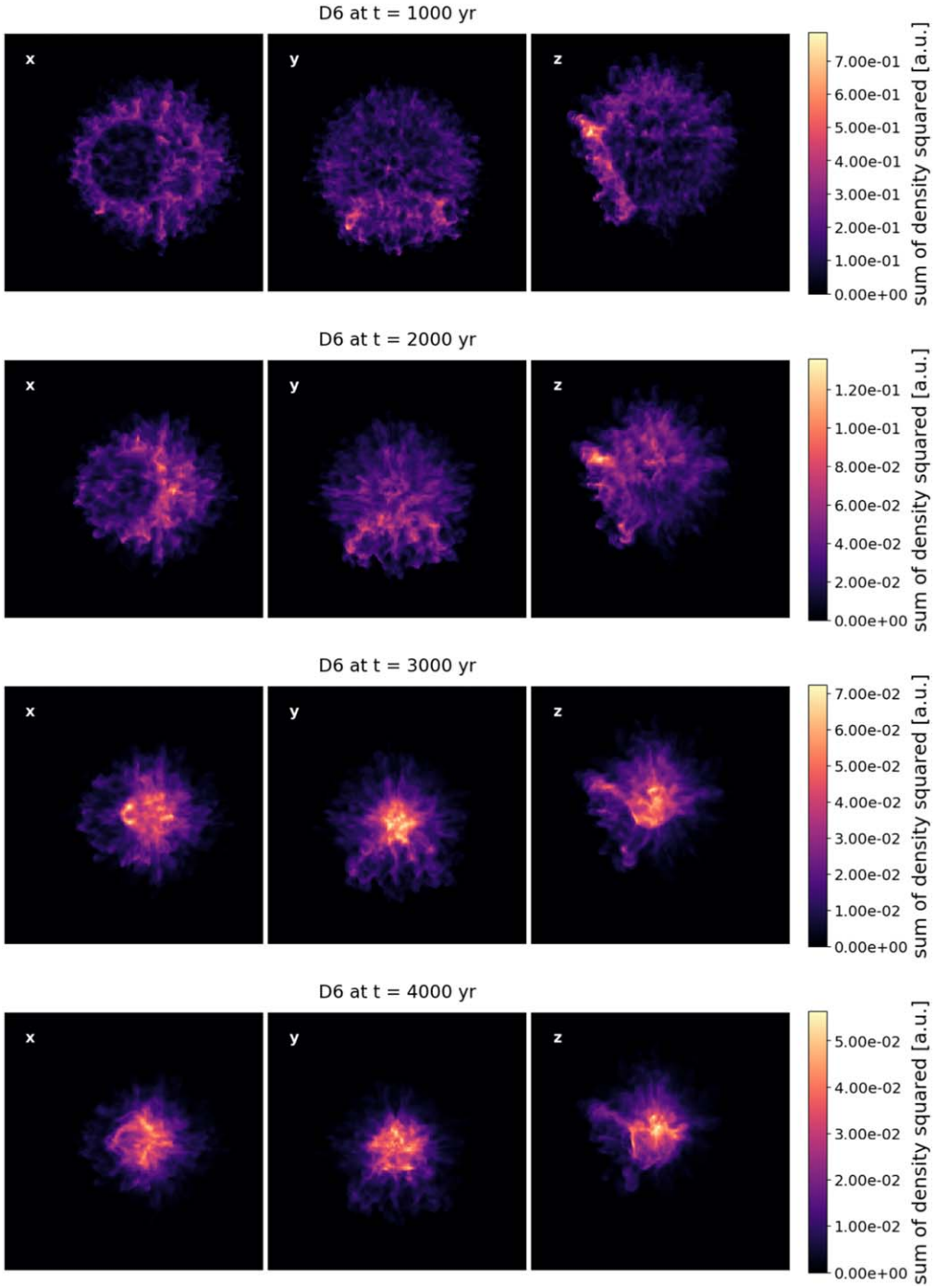

Figure 4. (Continued.)

density squared summed along the line of sight, the D^6 signature features are still visible at 500 yr, but become hidden at about 1000 yr. So one needs to separate the emission of the shocked ejecta and of the shocked ISM, which is possible using spatially resolved X-ray spectroscopy, as they have different compositions and thermodynamic states. In a subsequent paper focused on the thermal X-ray emission, we will present the separate contributions of the different media and of the different elements they contain. Furthermore, when particle acceleration happens, the induced nonthermal (synchrotron) emission traces the outline of the FS at X-ray wavelengths.

Wave fronts—The SNR shell is bounded by two shocks, the RS and the FS, while the ejecta and the ISM are separated by one interface, the CD. Spherical maps and angular spectra of the location of CD, RS, FS are shown in Figures 5, 6, 7, respectively, at select times, and movies from 1 yr to 4000 yr by steps of 1 yr are available online.[14] The spherical maps allow us to see at a glance the entire surface considered. The

[14] Note that the RS is not picked up by the shock tracking system during its final collapse to the center and after its rebound, even though it is visible in the slices and projections. Angular spectra are no longer reliable when this happens.

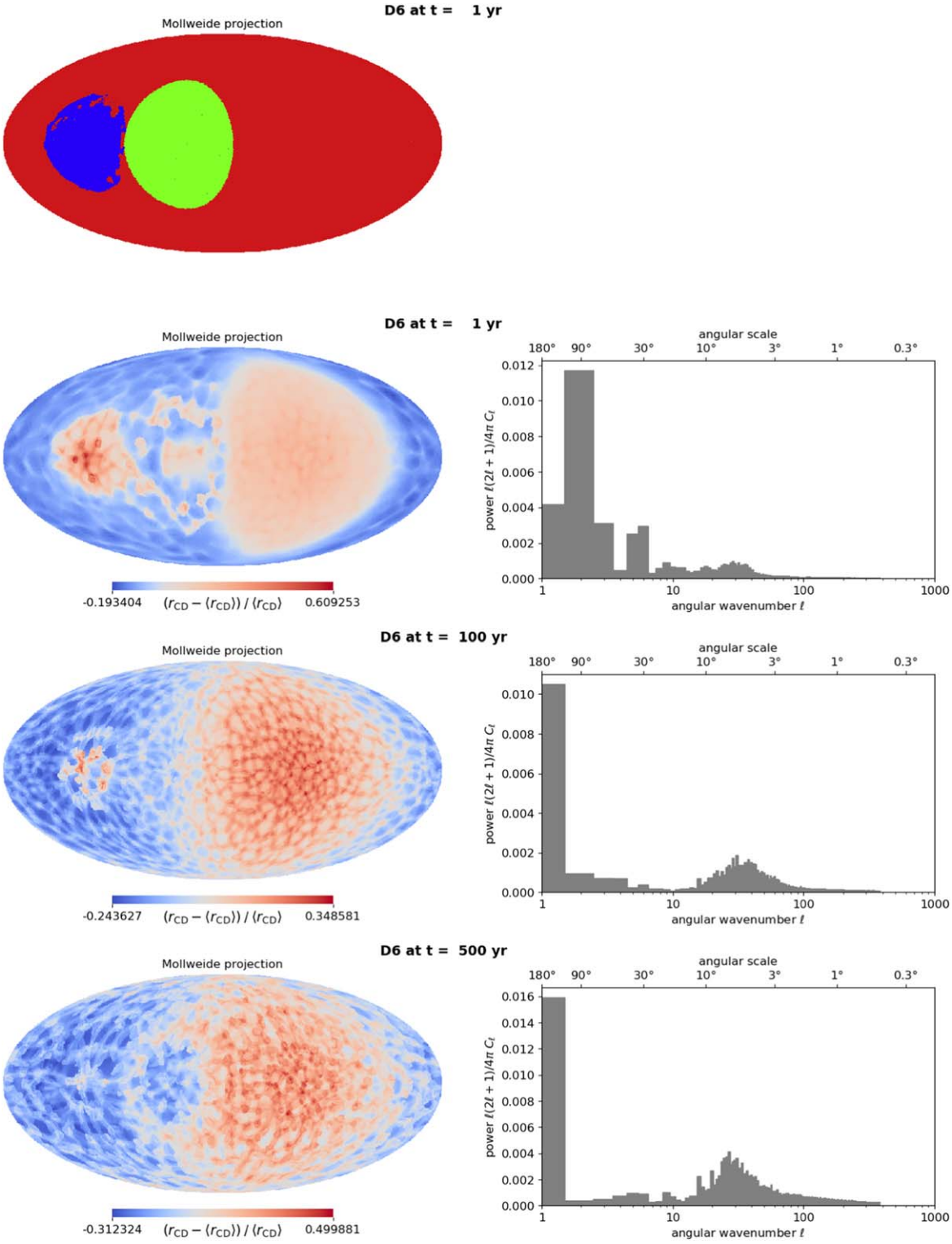

Figure 5. Morphology of the contact discontinuity. Maps on the left are spherical projections of the radial variations of the location of the wave. We use the Mollweide projection; for all times it is centered on the dipole component at the initial time. Spectra on the right result from an expansion in spherical harmonics of these variations. At angular wavenumber ℓ, the typical angular scale probed is π/ℓ, and the power C_ℓ plotted is normalized in such a way that each grayed bin is the contribution of wavenumber ℓ to the total variance of the radial fluctuations. Three times are shown: 1 yr, 100 yr, 500 yr. The maps and spectra evolve slowly after that. An animated version of this figure is available online, showing the evolution from 1 yr to 4000 yr by steps of 1 yr (the duration is 1 minute 20 s). The first plot is a color-coded mask to aid in identifying the origin of the features: red = regular ejecta, green cone = shadow from the companion, blue cylinder = tail from the first detonation. These masks are shown at $t = 1$ yr.

(An animation of this figure is available.)

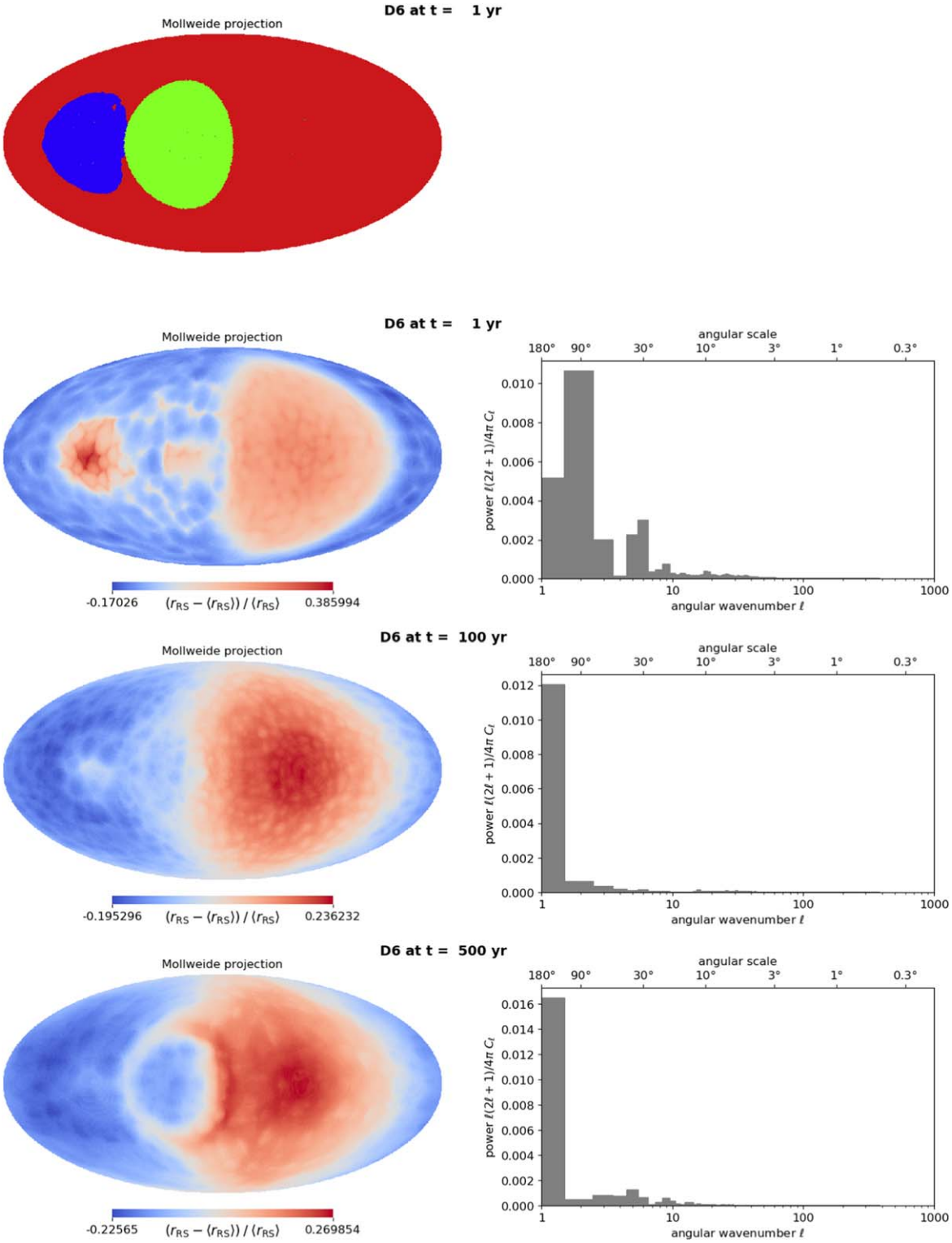

Figure 6. Morphology of the reverse shock. Same as Figure 5, for the radial variations of the RS location. Three times are shown: 1 yr, 100 yr, 500 yr. An animated version of this figure is available online, showing the evolution from 1 yr to 4000 yr by steps of 1 yr (the duration is 1 minute 20 s).

(An animation of this figure is available.)

angular spectra, as a function of the angular wavenumber ℓ, allow us to quantify which angular scales contribute to the overall morphology of the SNR. For each wave front we observe SN modes at large scales (small ℓ) that decay quickly in time, except for a permanent dipole ($\ell = 1$, meaning two-sided), which comes from the velocity shift from the binary motion. For the CD, we see that the RTI is growing from the smallest scales (largest ℓ) to larger scales (smaller ℓ), as

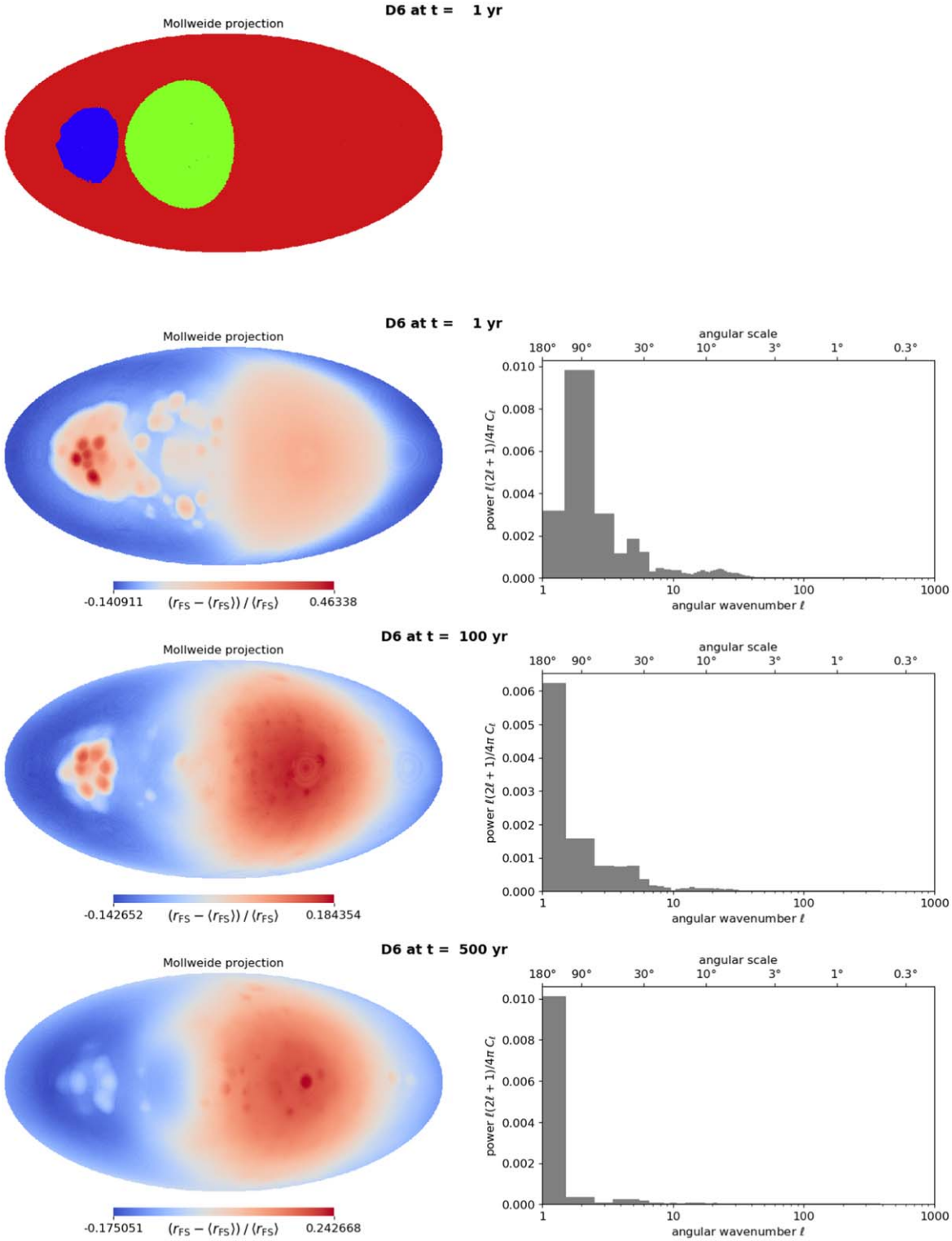

Figure 7. Morphology of the forward shock. Same as Figure 5, for the radial variations of the FS location. Three times are shown: 1 yr, 100 yr, 500 yr. An animated version of this figure is available online, showing the evolution from 1 yr to 4000 yr by steps of 1 yr (the duration is 1 minute 20 s).

(An animation of this figure is available.)

expected. In the first part of the simulation, the RTI spectral distribution is fairly symmetric, with a central peak slowly shifting to lower ℓ. After about 1000 yr, the distribution gets increasingly skewed toward lower ℓ, as finger growth is now driven by mergers. Maps for the RS and the FS are simpler than the ones for the CD, although they bear some imprint of the RTI as well: the feet of the fingers for the RS, the tips of the fingers for the FS. The tail from the first detonation is visible at

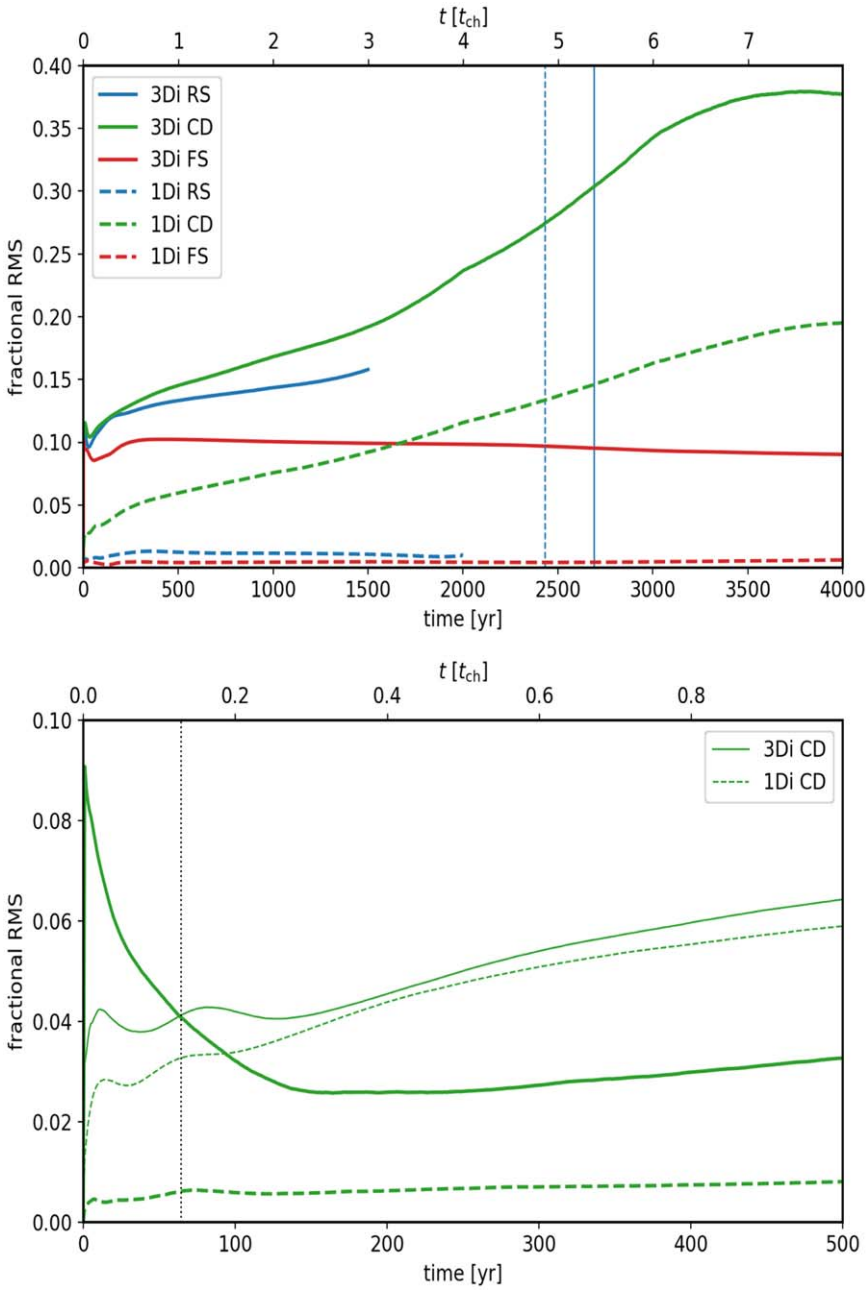

Figure 8. Fractional rms (square root of the angular power) as a function of time, for the three wave fronts: FS in red, CD in green, RS in blue. Time is indicated in years and in the characteristic timescale as defined by Equation (3). Two cases are compared: spherically symmetric ejecta (1Di, dashed curves) vs. asymmetric ejecta (3Di, solid lines). The top panel shows the evolution of the total power, for each interface, until the final simulation time of 4000 yr. The curves for the RS are stopped when the tracking of its surface, and therefore the calculated angular power becomes unreliable. The time when the RS reaches the center is indicated by the vertical blue line. The bottom panel shows the power separately at large scales, excluding the dipole ($1 < \ell < 10$, thick lines) and at small scales ($\ell \geqslant 10$, thin lines), only for the CD, and up to 500 yr after the explosion. The vertical dotted line indicates the time at which the two curves intersect for the 3Di simulation.

the beginning. Then the ring from the companion shadow appears, seen on the spectra in the low-ℓ modes.

As a final step, we aim to quantify which of the initial conditions (progenitor system and explosion mechanism) and of the ejecta–ISM interaction (growth of the RTI) shape the SNR at a given age. The summed angular power in the wave front deformations is shown in Figure 8 as a function of time. The top panel shows the evolution until the simulation end time 4000 yr, for each of CD, RS, FS, for both 1Di and 3Di cases. The 1Di case uses smooth initial conditions. For the FS and RS nothing is expected to happen and so this is merely a test of the numerical precision; for the CD this case shows the effect of purely the RTI. The 3Di case uses the actual initial profiles, and shows the imprint of the explosion. On the angular spectra, we see that the SN modes (at large scales) and the SNR modes (at small scales) can be separated for the first few hundred years around $\ell = 10$; the power in these two separate ℓ bands is plotted in the bottom panel, for the CD only, up to 500 yr. At small scales (excluding the permanent dipole, thin lines) the evolution is similar in the 1Di and 3Di cases, which comforts us in the fact that it corresponds to RTI growth. At large scales (thick lines), in 1Di nothing happens as expected, while in 3Di a decay is visible, strong initially but not reaching zero level. Looking at the 3Di case (solid lines), the low-ℓ and

high-ℓ curves for the CD intersect at 85 yr. It means that, after that time, most of the angular power in the ejecta morphology is coming from the SNR RTI, which is in its nonlinear phase of self-similar growth. However signatures of the explosion are still visible on the maps at much later ages, because they are localized in space, stable in time features. This is in contrast with our previous studies in Papers I and II with the N series of models, for which signatures were seen as statistical deviations across the entire SNR surface.

4. Discussion

We have presented for the first time the evolution and morphology of a D^6 SNR, up to 4000 yr after the explosion, which with our chosen ISM density is after all the ejecta have been shocked. In this section we discuss implications for the interpretation of observations of SNRs.

4.1. Other Effects

First we comment on aspects of our modeling that may be simplifications of the physical problem.

Effect of a different environment—We have deliberately used a very simple homogeneous ambient medium, in order to study the impact of the initial conditions. Certainly the ISM could be more complicated, especially after a few thousand years of evolution when the blast wave has covered tens of parsec, and that would impact the SNR as well. What we are demonstrating in this work, is that an inhomogeneous ISM is not required in order to produce a complex SNR morphology. The morphology we have been exploring is what is obtained, even in a uniform ISM, from the D^6 explosion physics. Type Ia SNRs are known to have more regular shapes overall than core-collapse SNRs (Lopez et al. 2011), but they do not necessarily have symmetric ejecta.

Effect of radioactive decay of ^{56}Ni—We investigated the effect of heating from radioactive decay with a simplified approach, as in Papers I and II.[15] We observed that heating tends to smooth the features, especially the central density peak, which thus may not be a robust feature. On projected maps, the main features we discussed in the previous section (tails from the first detonation, shadow from the companion) are still visible, just somewhat washed out. We recall that our simplified treatment, with local deposition of the available energy, provides the maximum possible impact of nickel decay. We note that centrally bright SNRs are observed: the so-called mixed-morphology SNRs (or thermal composites) that display radio shells with centrally peaked thermal X-rays, but these tend to be older objects and associated with massive star explosions (see the discussion in Paper II). It would be interesting to confirm whether some objects from this class originate from thermonuclear explosions.

4.2. Comparison with Previous Works

As mentioned in the introduction, only a few previous works have looked into the signature of a companion star on the SNR, some driven by observations (Lu et al. 2011; Vigh et al. 2011), others more theoretical in nature (García-Senz et al. 2012; Gray et al. 2016). We now compare our results to their findings.

García-Senz et al. (2012) ask whether there is "a hidden hole" in Type Ia SNRs. They perform 2D axisymmetric SPH simulations, which are also done in two steps, the SN then the SNR. Using an existing spherical model for the ejecta, they first compute the interaction of the ejecta with the companion, then remove the companion, scale up the ejecta, add a uniform ambient medium, and follow the SNR evolution from 28 yr to 1000 yr. They assume the companion to be a main-sequence solar-like star, and that it makes a "hole" in the ejecta up to a half-opening angle $\theta = 20°$, which is half the size of the ejecta shadow in our D^6 model.[16] They note that the hole can actually affect the SNR on larger angular scales. Their main finding is that the hole can remain open several hundred of years, which is consistent with our own findings. They report that RTI is enhanced at the edges of the hole, which we also observe in our simulations. They state that the hole is visible only along some directions, which we (and Gray et al. 2016 discussed next) disagree with, as in X-rays the entire SNR is observed in projection. In a follow-up paper (García-Senz et al. 2019) the study was complemented with 3D simulations plus a laser laboratory experiment.

Gray et al. (2016) investigate the "shadows" of Type Ia SNe companions. They perform 3D SPH simulations, also done in two steps, with the SNR evolution calculated from 100 yr (which is quite late for assuming free expansion) to 1000 yr (although results are shown only up to 300 yr). They assume the companion to be a subgiant star and find that it makes a shadow with half-opening angle of $\theta = 40°$, similar to the ejecta shadow in our D^6 model. They also find that the shadow is visible for hundreds of years. They compute a proxy for the thermal X-ray emission, and their maps in Figure 10 are to our knowledge the closest to our present work. As in our maps, the shadow is present at all viewing angles, with a different morphology depending on the direction of observation with respect to the shadow conical axis. Looking along the axis, a darker disk is observed on the surface of the remnant, and looking across the axis, a straight bright bar is observed at the edge of the remnant; in between an ellipse is observed, similar to what we obtained for D^6 (with a different kind of companion).

Lu et al. (2011) interpret some features seen in the X-ray images of Tycho's SNR as signatures of an (unseen) companion: a prominent arc would be a bow shock, and a darker region along the edge would be a shadow. The half-opening angle of the feature is about $\theta \simeq 10°$, which is significantly smaller than the shadow of the aforementioned models and of our D^6 model, although comparable with the size of the stream of stripped material. The paper offers no detailed modeling of the ejecta–companion interaction. The companion is assumed to be a normal star. Having presented evidence for the existence of a companion, the authors claim that this is evidence for the single degenerate scenario, which we now know is not correct: a double-degenerate explosion like D^6 can leave a surviving companion that can leave its imprint on the SNR.

It is worth noting that despite using different companion stars, in the numerical models discussed above, the angular size of the companion as seen from the explosion center is similar: in García-Senz et al. (2012), for a Sun-like companion, $\theta = 19.^{\circ}5$; in Gray et al. (2016), for more massive stars, θ

[15] Another radioactive element of interest to SN Ia is ^{44}Ti. However its yield is expected to be much smaller than that of ^{56}Ni, and it is not reliably calculated in our SN simulation.

[16] As there is actually matter everywhere, just less dense and more turbulent around the companion, we prefer to use the term "shadow" rather than "hole".

ranges in 24°–30°; and in our work, for a WD, $\theta = 22°$. The rough uniformity of angular size is a direct consequence of assuming mass transfer from the companion onto the primary. Assuming that the companion fills its Roche lobe at its orbital distance, its angular size is known to be a function of only the mass ratio q of the binary (Kopal 1959); $q = 0.6$ in our model. Using Eggleton (1983) formula, the angle $\theta = 10°$ inferred by Lu et al. (2011) would require q to be about 0.06, which seems unreasonably small. We also note that, being nonthermal, the X-ray arc in Tycho is more likely related to particle acceleration at the shock front.

Vigh et al. (2011) observe that Tycho's SNR has a two-sided, east/west morphology, like two hemispheres of slightly different radius. One of the possible causes they identify is mass loading from a companion star (other possibilities include an asymmetric wind of the progenitor). To assess this scenario, they perform hydro simulations, 2D axisymmetric and 3D, with varying opening angle and mass excess. They find that the morphology of Tycho can be reproduced with an opening angle of 90° (that is, an entire hemisphere) and a mass excess between 0.3 and 0.6 $M_\odot$. They produce mock X-ray maps (their Figure 9 and 11) that are not as realistic looking as ours or the ones of Gray et al. (2016). In a follow-up study (Moranchel-Basurto et al. 2020), they perform 3D MHD simulations and compute the synthetic synchrotron emission in radio. Whether or not it is appropriate to explain Tycho's SNR, this model is unlike a D^6 SNR.

4.3. Possible Target SNRs

Having described a D^6 SNR, it is natural to ask whether such a SNR has been observed or not. The sample of possible targets is quite limited. With current instruments, morphological studies are possible for SNRs located in our galactic neighborhood: the Milky Way and the Large and Small Magellanic Clouds (LMC and SMC). Plus we should look for SNRs that are dynamically young enough that their morphology be determined by the explosion rather than by the circumstellar medium. In the models investigated in Papers I and II, the imprint of the explosion was found to typically last for a few hundred years, though for D^6 it can last longer. There are only a handful of nearby SNRs known to be the remnants of Type Ia SNe and less than about a thousand years of age: G1.9 +0.3 (about 150 yr, Borkowski et al. 2013); SNR 0509–67.5 (about 400 yr, Warren & Hughes 2004; Rest et al. 2005); Kepler's SNR = SN 1604 = G4.5+6.8 (417 yr, Reynolds et al. 2007; Burkey et al. 2013), with a mysterious asymmetric morphology that must be giving us insights into the progenitor system (e.g., Kasuga et al. 2021); the aforementioned Tycho's SNR = SN 1572 = G120.1+1.4 (449 yr, Warren et al. 2005; Yamaguchi et al. 2017); SNR 0519–69.0 (about 450–600 yr, Kosenko et al. 2010; Rest et al. 2005); SN 1006 = G327.6 +14.6 (1015 yr, Uchida et al. 2013; Winkler et al. 2014); and N103B = SNR 0509–68.7 (less than 850 yr, Williams et al. 2018). We note that two of these SNRs, as observed in X-rays with Chandra, bear some similarity with our D^6 SNR: SNR 0519–69.0 looks mostly spherically symmetric except for a flatter section (similar to our model observed along the z-axis), N103B = SNR 0509–68.7 exhibits a darker circular region (similar to our model observed along the x-axis). Here we have to acknowledge the current limitations of both the simulations and the observations. Our simulations assume a clean environment; our maps are therefore an ideal case scenario. In the LMC and SMC, some SNRs have interesting features but are poorly resolved. We hope our work can help guide further careful analysis of nearby SNRs. We will dedicate a subsequent paper to spectroscopy diagnostics.

Finally, we note that one of the three hypervelocity WDs found by Shen et al. (2018b) points back to a recently found SNR candidate G70.0–21.5; however this scenario implies an explosion about 100,000 yr ago. This SNR is due for a more thorough X-ray study of the ejecta, but identifying the morphological features presented in this work will probably not be possible for such an old object.

5. Conclusion

In this paper, for the first time we have followed a "helium-ignited violent merger" or "dynamically driven double-degenerate double-detonation" (D^6) SN model into the SNR phase, up to 4000 yr after the explosion. We have analyzed the structure of the SNR using a variety of representations: 2D slices, 2D projections, 3D contours, and their angular variations. We have found that a D^6 progenitor system and explosion leave clear signatures on the SNR:

1. the first detonation produces an ejecta tail, which at early times looks like a protrusion from the shell;
2. the second detonation leaves a central density peak, which is revealed in X-rays when the RS reaches the center;
3. because of the initial velocity shift, the SNR shell is off-center at all times, which shows as a strong dipole component in the angular spectra;
4. the companion star generates a conical shadow in the ejecta, which is visible in projection as a dark patch surrounded by a bright ring.

Basically we found that the specific 3D structure of the explosion is preserved in the SNR phase. The features from the first detonation and from the companion are localized, and so the way they look depends on the direction of observation, producing various SNR morphologies. However, as we see all the shocked material in projection in X-rays, they should be visible to some degree along any orientation. The features from the shadow are long-lasting; they could in principle be detected in the shocked ejecta up to the time when the RS rebounds at the center of the SNR, which happens just short of 2700 yr after the explosion for an assumed density of 0.1 cm^{-3}. The conical shadow is visible on the SNR shell as a brighter ring encompassing a darker disk. The ring is a region of overgrowth of the RTI, while the disk is a region of undergrowth of it. This rather unusual SNR morphology is obtained even in a uniform ambient medium. So we point out that observing an irregular Type Ia SNR does not necessarily implies an inhomogeneous medium.

We emphasize that we have only one realization of the D^6 model. The size of the shadow may depend on the strength of the initial interaction between the ejecta and the companion, which may depend on the masses and explosion energy. The relative orientation between the tail from the first detonation and the conical shadow from the companion may also vary. For instance, the tail may happen to be aligned with the shadow, which may affect its evolution. Our work, which shows that the initial configuration matters in latter phases, should entice modelers to do more exhaustive studies of the D^6 scenario.

In a follow-up paper, we will conduct a more advanced study of the thermodynamical state of the plasma and its thermal emission, in order to allow for more precise comparisons of our simulation results with spatially and spectrally resolved X-ray observations. Our additional perspectives with D^6 modeling include, for the early phase, to study the nebular emission by means of radiative transfer calculations, and for the later phase, to study the visibility of the RS at and after its rebound. The later point warrants further study regarding its observability in SNRs, not just for D^6. Finally we would like to encourage searches for WDs in SNRs; D^6 is an example of a thermonuclear explosion with a surviving companion that is not a normal star.

This research has been supported by Grants-in-Aid for Scientific Research (16K17656, 19K03907). SN acknowledges the support by JSPS Grants-in-Aid for Scientific Research "KAKENHI" (A: grant No. JP19H00693) and Pioneering Program of RIKEN for Evolution of Matter in the Universe (r-EMU). This work was funded in part by the Interdisciplinary Theoretical and Mathematical Sciences (iTHEMS, https://ithems.riken.jp) program at RIKEN. S.S.H. acknowledges support by the Natural Sciences and Engineering Research Council of Canada (NSERC) and the Canadian Space Agency. We thank the anonymous referee for comments that helped clarify the manuscript.

Facilities: Simulation for the SN explosion was done on Oakforest–PACS at Joint Center for Advanced High Performance Computing and on Cray XC50 at Center for Computational Astrophysics, National Astronomical Observatory of Japan. Simulations for the SNR evolution were performed on the iTHEMS clusters at RIKEN.

Software: HEALPix (Gorski et al. 2005), SciPy (Virtanen et al. 2020), Matplotlib (Hunter 2007), VisIt (Childs et al. 2012).

ORCID iDs

Gilles Ferrand https://orcid.org/0000-0002-4231-8717
Ataru Tanikawa https://orcid.org/0000-0002-8461-5517
Donald C. Warren https://orcid.org/0000-0002-3222-9059
Shigehiro Nagataki https://orcid.org/0000-0002-7025-284X
Samar Safi-Harb https://orcid.org/0000-0001-6189-7665
Anne Decourchelle https://orcid.org/0000-0002-1796-758X

References

Benvenuto, O. G., Panei, J. A., Nomoto, K., Kitamura, H., & Hachisu, I. 2015, ApJL, 809, L6
Boehner, P., Plewa, T., & Langer, N. 2017, MNRAS, 465, 2060
Borkowski, K. J., Reynolds, S. P., Hwang, U., et al. 2013, ApJL, 771, 2
Burkey, M. T., Reynolds, S. P., Borkowski, K. J., & Blondin, J. M. 2013, ApJ, 764, 63
Cao, Y., Kulkarni, S. R., Howell, D. A., et al. 2015, Natur, 521, 328
Childs, H., Brugger, E., Whitlock, B., et al. 2012, VisIt: An End-User Tool for Visualizing and Analyzing Very Large Data, https://escholarship.org/uc/item/69r5m58v
Cioffi, D. F., McKee, C. F., & Bertschinger, E. 1988, ApJ, 334, 252
Dessart, L., Leonard, D. C., & Prieto, J. L. 2020, A&A, 638, A80
Di Stefano, R., Voss, R., & Claeys, J. S. W. 2011, ApJL, 738, L1
Dilday, B., Howell, D. A., Cenko, S. B., et al. 2012, Sci, 337, 942
Dwarkadas, V., & Chevalier, R. A. 1998, ApJ, 497, 807
Eggleton, P. P. 1983, ApJ, 268, 368
Ferrand, G., Decourchelle, A., Ballet, J., Teyssier, R., & Fraschetti, F. 2010, A&A, 509, L10
Ferrand, G., Decourchelle, A., & Safi-Harb, S. 2012, ApJ, 760, 34
Ferrand, G., Decourchelle, A., & Safi-Harb, S. 2014, ApJ, 789, 49
Ferrand, G., Warren, D. C., Ono, M., et al. 2019, ApJ, 877, 136
Ferrand, G., Warren, D. C., Ono, M., et al. 2021, ApJ, 906, 93
García-Senz, D., Badenes, C., & Serichol, N. 2012, ApJ, 745, 75
García-Senz, D., Velarde, P., Suzuki-Vidal, F., et al. 2019, ApJ, 871, 177
Garnavich, P. 2017, in Handbook of Supernovae, ed. A. W. Alsabti & P. Murdin (Cham: Springer), 2605
Gorski, K. M., Hivon, E., Banday, A. J., et al. 2005, ApJ, 622, 759
Gray, W. J., Raskin, C., & Owen, J. M. 2016, ApJ, 833, 62
Gronow, S., Collins, C., Ohlmann, S. T., et al. 2020, A&A, 635, A169
Gronow, S., Collins, C. E., Sim, S. A., & Röpke, F. K. 2021, A&A, 649, A155
Guillochon, J., Dan, M., Ramirez-Ruiz, E., & Rosswog, S. 2010, ApJL, 709, L64
Hachisu, I., Kato, M., & Nomoto, K. 2012, ApJL, 756, L4
Hillebrandt, W., Kromer, M., Röpke, F. K., & Ruiter, A. J. 2013, FrPhy, 8, 116
Hunter, J. D. 2007, CSE, 9, 90
Iben, I. J., & Tutukov, A. V. 1984, ApJS, 54, 335
Jha, S. W., Maguire, K., & Sullivan, M. 2019, NatAs, 3, 706
Ji, S., Fisher, R. T., García-Berro, E., et al. 2013, ApJ, 773, 136
Justham, S. 2011, ApJL, 730, L34
Kasen, D. 2010, ApJ, 708, 1025
Kashi, A., & Soker, N. 2011, MNRAS, 417, 1466
Kasuga, T., Vink, J., Katsuda, S., et al. 2021, ApJ, 915, 42
Kelly, P. L., Fox, O. D., Filippenko, A. V., et al. 2014, ApJ, 790, 3
Kerzendorf, W. E., Strampelli, G., Shen, K. J., et al. 2018, MNRAS, 479, 192
Kopal, Z. 1959, Close Binary Systems (London: Chapman & Hall)
Kosenko, D., Helder, E. A., & Vink, J. 2010, A&A, 519, A11
Kromer, M., Fremling, C., Pakmor, R., et al. 2016, MNRAS, 459, 4428
Kromer, M., Pakmor, R., Taubenberger, S., et al. 2013, ApJL, 778, L18
Li, W., Leaman, J., Chornock, R., et al. 2011, MNRAS, 412, 1441
Liu, Z.-W., Pakmor, R., Seitenzahl, I. R., et al. 2013, ApJ, 774, 37
Liu, Z.-W., & Zeng, Y. 2021, MNRAS, 500, 301
Lopez, L. A., Ramirez-Ruiz, E., Huppenkothen, D., Badenes, C., & Pooley, D. A. 2011, ApJ, 732, 114
Lu, F. J., Wang, Q. D., Ge, M. Y., et al. 2011, ApJ, 732, 11
Maeda, K., Kutsuna, M., & Shigeyama, T. 2014, ApJ, 794, 37
Maoz, D., Mannucci, F., & Nelemans, G. 2014, ARA&A, 52, 107
Marietta, E., Burrows, A., & Fryxell, B. 2000, ApJS, 128, 615
Marion, G. H., Brown, P. J., Vinkó, J., et al. 2016, ApJ, 820, 92
Moranchel-Basurto, A., Velázquez, P. F., de Parga, G. A., et al. 2020, MNRAS, 1538, 1531
Nomoto, K. 1982, ApJ, 257, 780
Nomoto, K., & Kondo, Y. 1991, ApJL, 367, L19
Pakmor, R., Hachinger, S., Röpke, F. K., & Hillebrandt, W. 2011, A&A, 528, A117
Pakmor, R., Kromer, M., Taubenberger, S., et al. 2012, ApJL, 747, L10
Pakmor, R., Kromer, M., Taubenberger, S., & Springel, V. 2013, ApJL, 770, L8
Pakmor, R., Röpke, F. K., Weiss, A., & Hillebrandt, W. 2008, A&A, 489, 943
Pakmor, R., Zenati, Y., Perets, H. B., & Toonen, S. 2021, MNRAS, 503, 4734
Pan, K.-c., Ricker, P. M., & Taam, R. E. 2012, ApJ, 750, 151
Papish, O., Soker, N., García-Berro, E., & Aznar-Siguán, G. 2015, MNRAS, 449, 942
Petruk, O., Kuzyo, T., Orlando, S., Pohl, M., & Brose, R. 2021, MNRAS, 505, 755
Polin, A., Nugent, P., & Kasen, D. 2019, ApJ, 873, 84
Polin, A., Nugent, P., & Kasen, D. 2021, ApJ, 906, 65
Rest, A., Suntzeff, N. B., Olsen, K., et al. 2005, Natur, 438, 1132
Reynolds, S. P. 2017, in Handbook of Supernovae, ed. A. W. Alsabti & P. Murdin (Cham: Springer), 1981
Reynolds, S. P., Borkowski, K. J., Hwang, U., et al. 2007, ApJL, 668, L135
Ruiter, A. J. 2020, in IAU Symp. 357, White Dwarfs as Probes of Fundamental Physics: Tracers of Planetary, Stellar and Galactic Evolution, ed. M. A. Barstow (Cambridge: Cambridge Univ. Press), 1
Ruiz-Lapuente, P. 2019, NewAR, 85, 101523
Saio, H., & Nomoto, K. 1985, A&A, 150, L21
Sato, Y., Nakasato, N., Tanikawa, A., et al. 2015, ApJ, 807, 105
Sato, Y., Nakasato, N., Tanikawa, A., et al. 2016, ApJ, 821, 67
Schulreich, M. M., & Breitschwerdt, D. 2022, MNRAS, 509, 716
Schwab, J., Shen, K. J., Quataert, E., Dan, M., & Rosswog, S. 2012, MNRAS, 427, 190
Shen, K. J., Blondin, S., Kasen, D., et al. 2021, ApJL, 909, L18
Shen, K. J., Boubert, D., Gänsicke, B. T., et al. 2018b, ApJ, 865, 15
Shen, K. J., Kasen, D., Miles, B. J., & Townsley, D. M. 2018a, ApJ, 854, 52
Shen, K. J., & Schwab, J. 2017, ApJ, 834, 180
Sim, S. A., Röpke, F. K., Hillebrandt, W., et al. 2010, ApJL, 714, 52
Tanikawa, A., Nakasato, N., Sato, Y., et al. 2015, ApJ, 807, 40

Tanikawa, A., Nomoto, K., & Nakasato, N. 2018, ApJ, 868, 90
Tanikawa, A., Nomoto, K., Nakasato, N., & Maeda, K. 2019, ApJ, 885, 103
Taubenberger, S., Kromer, M., Pakmor, R., et al. 2013, ApJL, 775, L43
Teyssier, R. 2002, A&A, 385, 337
Timmes, F. X., Hoffman, R. D., & Woosley, S. E. 2000, ApJS, 129, 377
Timmes, F. X., & Swesty, F. D. 2000, ApJS, 126, 501
Uchida, H., Yamaguchi, H., & Koyama, K. 2013, ApJ, 771, 56
Vigh, C. D., Velázquez, P. F., Gómez, D. O., et al. 2011, ApJ, 727, 32
Vink, J. 2017, in Handbook of Supernovae, ed. A. W. Alsabti & P. Murdin (Cham: Springer), 2063
Virtanen, P., Gommers, R., Oliphant, T. E., et al. 2020, NatMe, 17, 261
Warren, D. C., & Blondin, J. M. 2013, MNRAS, 429, 3099
Warren, J. S., & Hughes, J. P. 2004, ApJ, 608, 261
Warren, J. S., Hughes, J. P., Badenes, C., et al. 2005, ApJ, 634, 376
Webbink, R. F. 1984, ApJ, 277, 355
Whelan, J., & Iben, I. J. 1973, ApJ, 186, 1007
Williams, B. J., Blair, W. P., Borkowski, K. J., et al. 2018, ApJL, 865, L13
Winkler, P. F., Williams, B. J., Reynolds, S. P., et al. 2014, ApJ, 781, 65
Yamaguchi, H., Hughes, J. P., Badenes, C., et al. 2017, ApJ, 834, 124
Zeng, Y., Liu, Z.-W., & Han, Z. 2020, ApJ, 898, 12